Depth-resolved resonant inelastic x-ray scattering at a superconductor/half-metallic-ferromagnet interface through standing wave excitation

Cheng-Tai Kuo,[1,2,*] Shih-Chieh Lin,[1,2] Giacomo Ghiringhelli,[3] Yingying Peng,[3,†] Gabriella Maria De Luca,[4] Daniele Di Castro,[5] Davide Betto,[6] Mathias Gehlmann,[1,2] Tom Wijnands,[7] Mark Huijben,[7] Julia Meyer-Ilse,[2] Eric Gullikson,[2] Jeffrey B. Kortright,[2] Arturas Vailionis,[8] Nicolas Gauquelin,[7,9] Johan Verbeeck,[9] Timm Gerber,[1,2,10] Giuseppe Balestrino,[5] Nicholas B. Brookes,[6] Lucio Braicovich,[3] and Charles S. Fadley[1,2,‡]

[1]*Department of Physics, University of California Davis, Davis, California 95616, USA*

[2]*Materials Sciences Division, Lawrence Berkeley National Laboratory, Berkeley, California 94720, USA*

[3]*CNR-SPIN and Dipartimento di Fisica Politecnico di Milano, Piazza Leonardo da Vinci 32, Milano I-20133, Italy*

[4]*Dipartimento di Fisica "E. Pancini" Università di Napoli 'Federico II' and CNR-SPIN, Complesso Universitario di Monte Sant'Angelo, via Cinthia, Napoli I-80126, Italy*

[5]*CNR-SPIN and Dipartimento di Ingegneria Civile e Ingegneria Informatica, Università di Roma Tor Vergata, Via del Politecnico 1, I-00133 Roma, Italy*

[6]*European Synchrotron Radiation Facility, 71 Avenue des Martyrs, CS40220, F-38043 Grenoble Cedex 9, France*

[7]*Faculty of Science and Technology and MESA+ Institute for Nanotechnology, University of Twente, Enschede 7500 AE, The Netherlands*

[8]*Stanford Nano Shared Facilities, Stanford University, Stanford, California 94305, USA*

[9]*Electron Microscopy for Materials Science (EMAT), University of Antwerp, Groenenborgerlaan 171, B-2020 Antwerp, Belgium*

[10]*Peter Grünberg Institut PGI-6, Research Center Jülich, 52425 Jülich, Germany*

(Received 27 August 2018; revised manuscript received 20 November 2018; published 21 December 2018)

We demonstrate that combining standing wave (SW) excitation with resonant inelastic x-ray scattering (RIXS) can lead to depth resolution and interface sensitivity for studying orbital and magnetic excitations in correlated oxide heterostructures. SW-RIXS has been applied to multilayer heterostructures consisting of a superconductor $La_{1.85}Sr_{0.15}CuO_4$ (LSCO) and a half-metallic ferromagnet $La_{0.67}Sr_{0.33}MnO_3$ (LSMO). Easily observable SW effects on the RIXS excitations were found in these LSCO/LSMO multilayers. In addition, we observe different depth distribution of the RIXS excitations. The magnetic excitations are found to arise from the LSCO/LSMO interfaces, and there is also a suggestion that one of the *dd* excitations comes from the interfaces. SW-RIXS measurements of correlated-oxide and other multilayer heterostructures should provide unique layer-resolved insights concerning their orbital and magnetic excitations, as well as a challenge for RIXS theory to specifically deal with interface effects.

DOI: 10.1103/PhysRevB.98.235146

Resonant inelastic x-ray scattering (RIXS) is a photon-in/photon-out synchrotron-based spectroscopy that has been shown to uniquely probe the charge transfer, *dd*, magnetic, phonon, and other excitations in correlated oxides and other systems, and has been extensively reviewed elsewhere [1,2]. RIXS is considered to be a probe of bulk properties, at depths of the order of 1000 Å, although, in fact, the penetration and escape depths of the resonant x rays can be significantly reduced for excitations at a strong absorption edge of a majority elemental constituent [3], and thus the actual sensing depth is somehow ill defined and variable from sample to sample. It would thus be desirable to give RIXS more quantitative depth sensitivity, for example to investigate interfaces in oxide heterostructures, which are known to show emergent properties (e.g., two-dimensional (2D) electron gases, interface-induced ferromagnetism) not present in the single constituents [4], with these triggering intense interest and many publications on various oxide interfaces [5]. Here we demonstrate that by using standing wave (SW) excitation from multilayer heterostructures, interface-specific RIXS information can be achieved.

It is well known that a strong Bragg reflection from a multilayer heterostructure or a single crystal creates a SW inside and above the sample, and that it can be used to excite x-ray or photoelectron emission with resulting depth resolution [6–11]. Prior reviews of these developments using multilayer reflection from members of our group provide additional background [12–15], including a detailed discussion of the x-ray optical theoretical modeling program that we will use to interpret our data: Yang X-ray Optics (YXRO) [3]. The relevant Bragg equation is $n\lambda_x = 2d_{ML}\sin\theta_{\rm inc}$, where n is the order of the reflection, λ_x is the x-ray wavelength, d_{ML} is the bilayer repeat spacing in the multilayer, and $\theta_{\rm inc}$ is the incidence angle relative to the multilayer. It is simple to show that for first-order Bragg reflection, the period of the SW electric-field intensity $|E^2| \equiv \lambda_{SW} = d_{ML}$, where λ_{SW} is the wavelength of the SW vertical to the layers and the interfaces

*Corresponding author: chengtaikuo@lbl.gov

†Present address: Department of Physics and Seitz Materials Research Laboratory, University of Illinois, Urbana, Illinois 61801, USA.

‡Corresponding author: fadley@lbl.gov

between them. The SW can be swept through the sample in two principal ways: scanning the incidence angle $\theta_{\rm inc}$ over the Bragg reflection through a rocking curve (the method used here) and scanning the photon energy, i.e., the photon wavelength λ_x through the Bragg reflection. When spanning the whole Bragg peak, both methods shift the SW spatially by one-half of its period in a direction perpendicular to the interfaces in the multilayer. The standard formula for the SW intensity at a given depth z below the surface is

$$I(\theta_{\rm inc}) \propto 1 + R(\theta_{\rm inc}) + 2\sqrt{R(\theta_{\rm inc})} f \cos[\varphi(\theta_{\rm inc}) - 2\pi(z/\lambda_{SW})], \quad (1)$$

where $R(\theta_{\rm inc})$ is the reflectivity, f is the fraction of atoms in coherent positions for Bragg reflection, $\varphi(\theta_{\rm inc})$ is the phase difference between incident and scattered waves, and z/λ_{SW} is the vertical position of a given layer or interface of interest, as normalized to the SW period. The third term here represents the SW modulation. Although the basic physics of the SW formation is contained in Eq. (1), the YXRO program actually calculates the SW in a more accurate way, including x-ray attenuation and multiple scattering or dynamical diffraction effects [3].

In this work, we show that SW excitation in RIXS can be used to provide enhanced depth and interface sensitivity to the technique. We have chosen to probe the interface between the superconducting cuprate $La_{1.85}Sr_{0.15}CuO_4$ (LSCO) and the half-metallic-ferromagnetic manganite $La_{0.67}Sr_{0.33}MnO_3$ (LSMO) in an assessment of SW-RIXS capabilities. In this cuprate/manganite heterostructure, De Luca *et al.* found a strong charge transfer from Mn to Cu ions using electron energy loss spectroscopy and x-ray circular dichroism [16]. The interfacial CuO_2 planes of the cuprate develop weak ferromagnetism associated with the charge transfer from the MnO_2 planes of the manganite, and the Dzyaloshinskii-Moriya interaction propagates the magnetization from the interfacial CuO_2 planes into the superconductor, leading to a depression of its superconducting critical temperature. Information on the length scale of this charge transfer at the LSCO/LSMO interface and its relationship to the *dd* and magnetic excitations could provide a more complete understanding of this interface coupling, with LSCO/LSMO thus providing an ideal system for testing the depth resolution of SW-RIXS.

Multilayers of $(LSCO_n/LSMO_m)_p$ [$n = 2$ unit cell (uc), $m = 7$ uc, and $p = 20$ repeats] were grown by pulsed laser deposition, either on SrO-terminated or on TiO_2-terminated $SrTiO_3$ (STO) substrates, *in situ* controlled by reflection high-energy electron diffraction. The details of the growth of the LSCO/LSMO heterostructures can be found elsewhere [16,17]. The individual layers are thus nominally LSCO = 26.4 Å and LSMO = 27.0 Å, based on bulk properties, yielding an estimated d_{ML} of 53.4 Å. More precise measurements of these dimensions using scanning transmission electron microscopy, together with high-angle annular dark field imaging (STEM-HAADF) and electron energy loss spectroscopy (EELS) were performed on a Titan 80–300 microscope equipped with an aberration corrector for the probe forming lens used at 300 kV acceleration voltage with a 20 mrad convergence angle and a collection half-angle of 40–95 mrad for HAADF imaging. EELS was used to determine the chemistry at each LSMO(top)/LSCO(bottom) and LSCO(top)/LSMO(bottom) interface, which always consist of the sequence -$La_{0.9}Sr_{0.1}O$-$La_{0.9}Sr_{0.1}O$-CuO_2-$La_{0.66-x}Sr_{0.33+x}O$-MnO_2-$La_{0.66}Sr_{0.33}O$- and -$La_{0.66}Sr_{0.33}O$-MnO_2-$La_{0.9-x}Sr_{0.1+x}O$-CuO_2-$La_{0.9}Sr_{0.1}O$-$La_{0.9}Sr_{0.1}O$-, respectively ($0 < x < 0.15$). La/Sr ratios are subject to a 5% error inherent to the measurement method. One aspect of this data is shown in Figs. 1(d) and 1(e), in which the TiO_2 termination is shown to be less regular as a multilayer. Therefore, we present in the main text the results on the SrO-terminated multilayer, which has superior structural regularity, and discuss in detail the TiO_2-terminated case in our Supplemental Material [18] because the SW effects on RIXS were more complex to analyze due to irregularities in its bilayer spacings as seen in STEM images. The SW-RIXS measurements on both samples were performed at ID32 of ESRF using the high-resolution ERIXS spectrometer [19]. The total instrumental energy resolution was set at 70 meV, determined as the FWHM of the nonresonant diffuse scattering from silver paint adjacent to the sample. The multilayer samples were cooled down to ∼20 K by liquid He, and thus below the superconducting T_c of bulk LSCO (∼30–40 K), and the ferromagnetic T_c of bulk LSMO (∼270–298 K). The RIXS data were collected near the Cu L_3 edge.

Given the multilayered structure of the sample, as shown in Fig. 1(a), we can choose the incidence angle $\theta_{\rm inc}$ to match the Bragg conditions near the Cu L_3 edge ($h\nu = 931.2$ eV) for the sample period $d_{ML} \approx 53.4$ Å. From the measured imaginary part of the index of refraction for the multilayer (see Supplemental Material [18]), we estimate the effective exponential decay length of the x-ray intensity, including incidence and exit, to be about $\Lambda_{x,\rm eff} \approx 54$ Å, which is drastically lower than the ∼1000 Å that are often assumed in the literature, due to the strong absorption resonance. Coincidentally, the decay length approximately matches the bilayer period, which means that the RIXS signal is almost completely attenuated at the bottom of the multilayer at a depth of 20 periods or ∼1070 Å. Indeed, 95% of the RIXS signal arises from a depth of $3\Lambda_{x,\rm eff} \approx$ 162 Å or about the three topmost bilayers. As noted above, for first-order Bragg reflection, the SW period $\lambda_{SW} = d_{ML}$, and by scanning $\theta_{\rm inc}$ in the vicinity of the nominal Bragg position, the maxima of the SW moves by $\lambda_{SW}/2 \approx 27$ Å across the interface. Other details concerning the characterization of the sample grown on SrO-terminated STO, as well as the second one grown on TiO_2-terminated STO, are presented in the Supplemental Material [18].

The intensities of the individual RIXS excitations as a function of incidence angle, which we call rocking curves (RCs), are thus modulated by the moving SW field, schematically shown in Figs. 1(a) and 1(b). Figure 1(b) shows the scattering geometry in real space and momentum space. The incident beam hits the sample at an angle $\theta_{\rm inc} \approx 7^\circ$ from the surface and is reflected by the multilayer with a Bragg vector $\mathbf{q}_{SW}$ normal to the surface; the RIXS signal is collected in backscattering at $\theta_{\rm scatt} \approx 30^\circ$, resulting in a RIXS scattering vector $\mathbf{q}_{\rm RIXS}$ mostly parallel to the surface. Throughout the RC, which means with increasing $\theta_{\rm inc}$ and q_{SW}, the standing wave develops initially in the

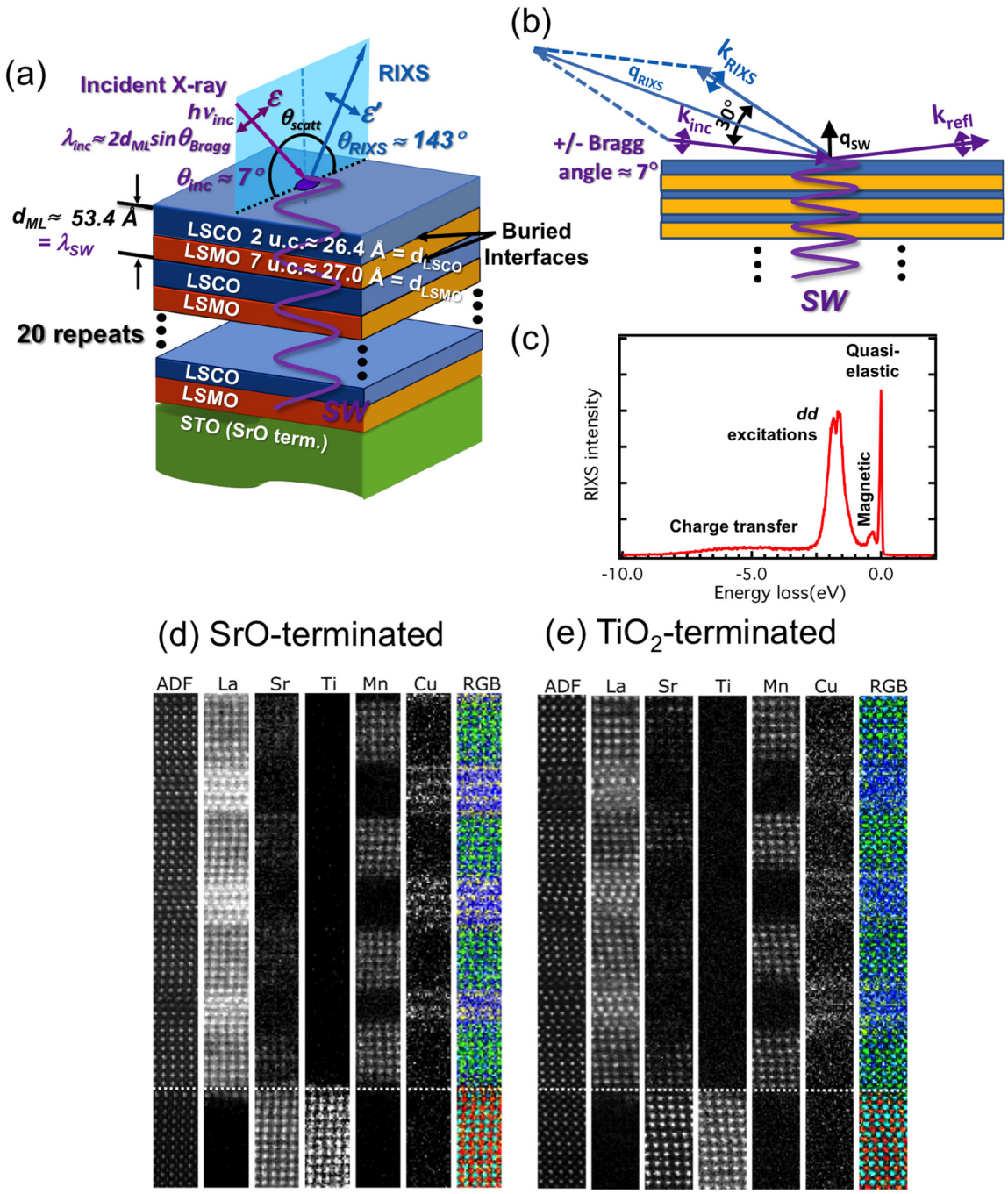

FIG. 1. Schematic illustrations of the standing wave (SW) excited resonant inelastic x-ray scattering (RIXS) measurement. (a) Diagram of the multilayer sample with bilayer period d_{ML}, including the geometry of the exciting x-ray beam, the scattered photons, and the standing wave indicated. The multilayer samples consist of 20 bilayers of 2 unit cells of $La_{1.85}Sr_{0.15}CuO_4$ (LSCO) and 7 unit cells of $La_{0.67}Sr_{0.33}MnO_3$ (LSMO), grown epitaxially on an SrO-terminated STO substrate. The dimensions shown are nominal, based on bulk lattice parameters. (b) The SW-RIXS experimental geometry in real space and momentum space. (c) A typical RIXS spectrum, from the SrO-terminated growth, that exhibits quasielastic, magnetic, and dd excitations. (d),(e) The STEM-HAADF and EELS results near the initial growth on STO for both the SrO-terminated growth and the less regular TiO_2-terminated growth. In the RBG images, Ti is orange, Mn is green, Cu is blue, Sr is turquoise, and La is green.

low-absorption LSMO layer and shifts by $d_{ML}/2$ into the LSCO layer as the multilayer Bragg peak is crossed. Figure 1(c) shows a representative Cu L_3 edge RIXS spectrum from the SrO-terminated LSCO/LSMO multilayer, and it is clear that quasielastic, magnetic, and dd excitations are observed. The RIXS spectrum in the range of 0 to 500 meV consists of the elastic peak, phonon excitations, and magnetic (mainly single magnon and bimagnon) excitations [20–25]. The bimagnon signal in RIXS results from the sudden change of the superexchange magnetic interaction in the intermediate state [26,27]. The spectral range from 1 to 2.5 eV is dominated by dd excitations [2,21–23,28], which are partly resolved into

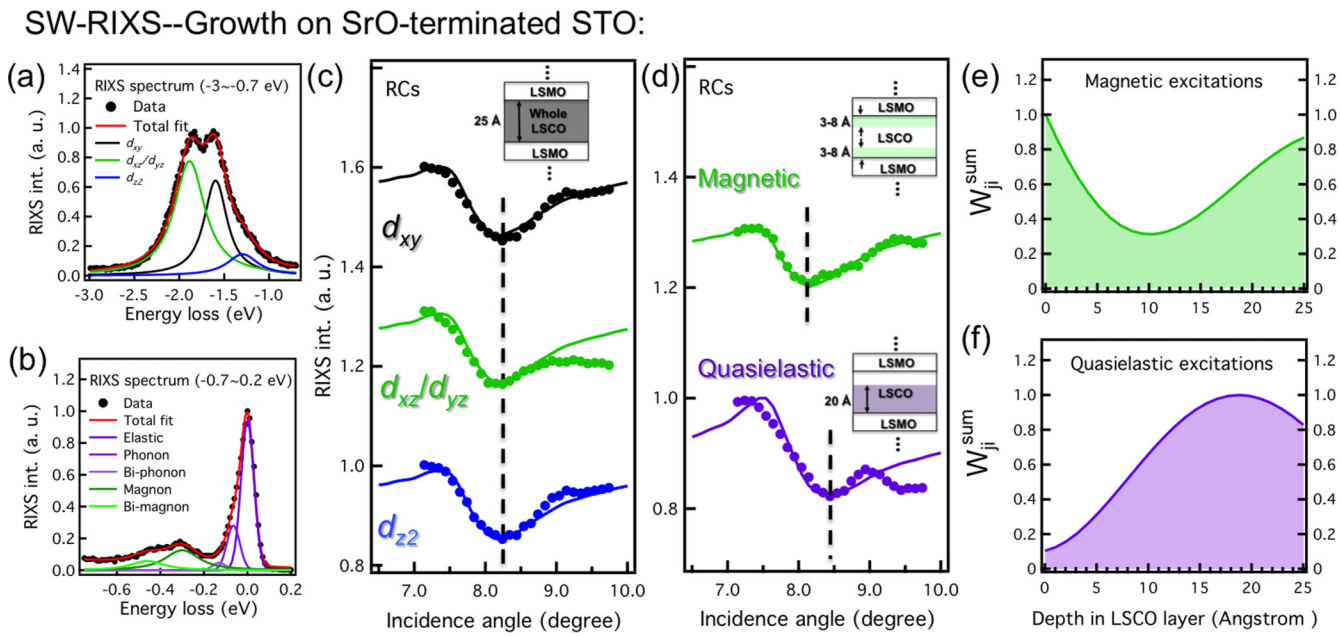

FIG. 2. SW-RIXS of various excitations for growth on SrO-terminated STO. RIXS spectra of (a) dd excitations and (b) quasielastic and magnetic excitations. The dd excitations have three components: d_{xy}, d_{xz}/d_{yz}, and d_{z2}. The quasielastic intensity includes three components: the zero-loss or elastic line and phonon excitations, with these three components being summed to give the rocking curve (RC). The magnetic spectra are fit with two components (magnon and bimagnon), whose intensities are summed to yield the magnetic RC. (c) The experimental dd-excitation RCs (data points) together with YXRO calculations (lines). (d) The experimental RCs for the magnetic and quasielastic excitations (data points) together with YXRO calculations (lines). (e) The summed weighting factors from Eq. (2) for the magnetic excitations. (f) The summed weighting factors from Eq. (2) for the quasielastic excitations.

a doublet and a low-energy shoulder whose assignment was already discussed in Ref. [29]. Here we focus on the RCs of the dd, magnetic, and quasielastic (elastic + phonon) RIXS excitations from the SrO-terminated multilayer, although noting that at our resolutions, cleanly separating them all by peak fitting must be done carefully to avoid artifacts.

First, we discuss the RCs of the dd excitations. The dd excitations can be ascribed to the transfer of the $3d$ hole from the $d_{x^2-y^2}$ orbital to the d_{z2}, d_{xy}, and d_{yz}/d_{xz} orbitals [28]. In Fig. 2(a), the dd excitations are deconvoluted by peak fitting into the d_{z2}, d_{xy}, and d_{yz}/d_{xz} components. In order to observe the SW movement across the interfaces, the RIXS dd excitation spectra were collected while varying the incidence angle between 7.2° and 9.7°, thus yielding three RCs shown in Fig. 2(c). All the experimental and theoretical RCs are normalized to a maximum of unity and are offset vertically for readability. The fractional modulation of each RC can thus be read directly from the ordinate scale. The intensity of all dd excitations is modulated by 15–20%, meaning that the SW has a clear influence on the RIXS process: this is the experimental demonstration that SW-RIXS is feasible. We note also that these three RCs show a very similar shape, with intensity minima at ∼8.2°, thus indicating a very similar depth distribution. This is not surprising, as the cross section of the dd excitations is not expected to depend on the details of the local coordination of the Cu^{2+} ions; at most, their energy might change from the surface to the bulk layers, but in this experiment we did not attempt to detect those energy shifts, as these are expected to be small. One can argue that normalization to the "flat" wings of an RC for which reflectivity and SW modulation are minimal is a better choice, but it can be more difficult to do if instrumental effects such as beam movement along the sample or slight changes in self-absorption or excitation cross section during a scan lead to a complex, sloping background. Our normalization choice should not affect any of our conclusions, however. We illustrate this in Figs. 3(d) and 3(e), where we show the measured and calculated reflectivity, and its second derivative. It seems clear that no significant SW effects exist at the edges of the 7.0–9.5° angle of our experimental RCs [Figs. 2(c) and 2(d)] and calculated RCs [Fig. 3(c)].

As the RC intensity modulation is significant, we now try to relate these RCs to an approximate depth distribution of the loss processes involved, by simulating the RIXS process using the previously mentioned YXRO program [3]. Two key inputs to this program are the resonant index of refraction and the detailed structure (e.g., thickness of individual layers) of the sample. The resonant index of refraction has been derived by measuring the multilayer x-ray absorption curve and using Kramers-Kronig analysis (see Supplemental Material [18]). Note that all of the resonant Cu atoms are assumed to be uniform in the calculations. It is possible that the Cu atoms near the top and bottom interfaces have different environments (e.g., position distortions, charge transfer, etc.). This could lead to the difference in the x-ray absorption and a slight change in the simulated SW electric-field distribution, but it will not change the conclusions of this work. Future SW work on deriving more interface-like x-ray absorption should help improve our understanding of the x-ray optical effects in RIXS.

The thicknesses of the individual LSCO and LSMO layers are determined from high-resolution STEM-HAADF images

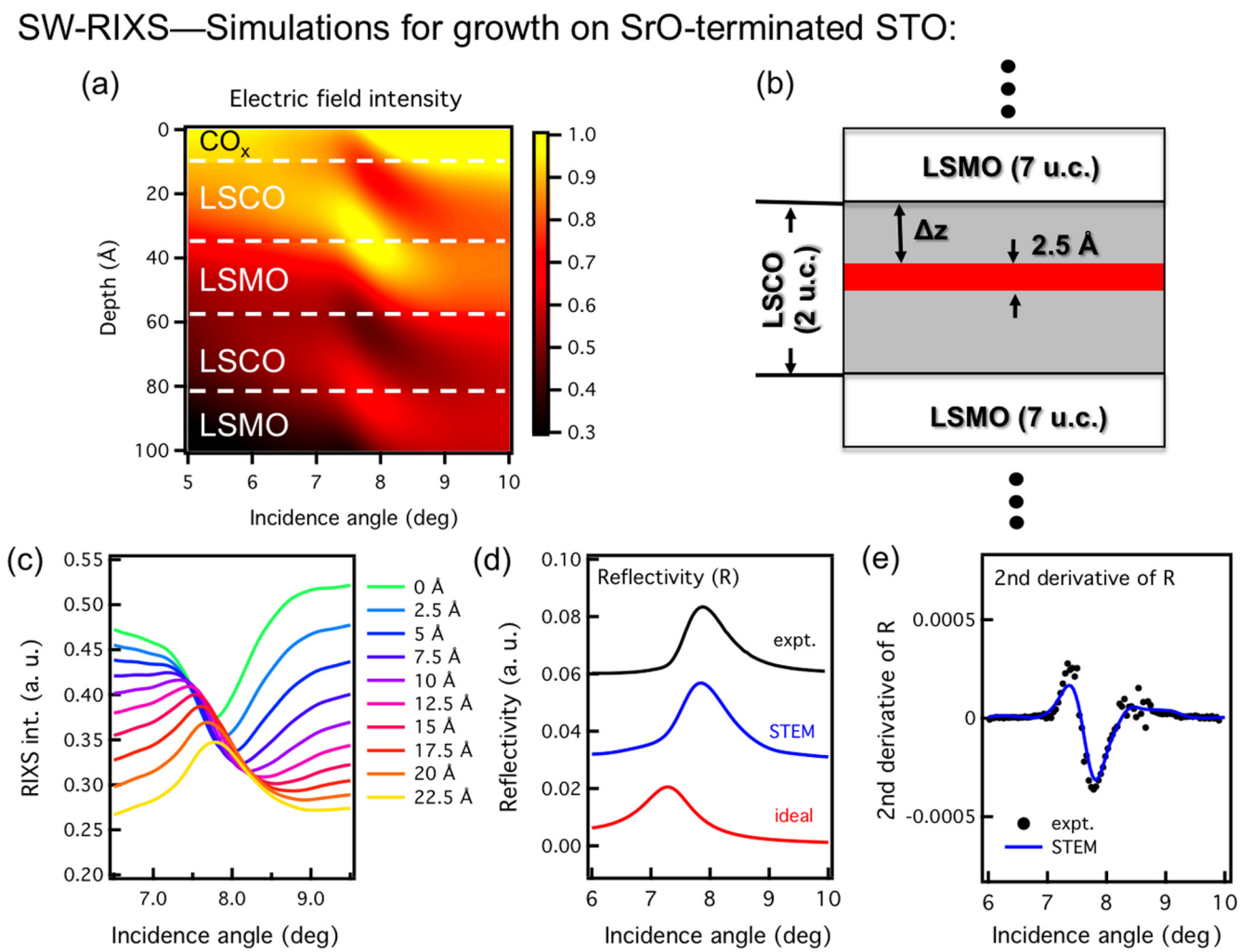

FIG. 3. (a)–(c) Results of x-ray optical simulations of the SW effects and the depth-resolved RCs, for growth on SrO-terminated STO. (a) The depth and incidence-angle dependence of the SW electric-field intensity $|E(z, \theta_{\rm inc})|^2$. Note in particular the movement of the SW through the top two LSCO-top/LSMO-bottom interfaces. (b) The model sample profile of LSCO that is used to simulate the RCs resulting from 0 to 22.5 Å, with "delta-layer" thickness of 2.5 Å. (c) The calculated RCs for various Δz values. (d) Experimental (black curve) and calculated (blue and red curves) soft x-ray reflectivity. (e) Experimental (black dots) and calculated second derivative of the reflectivity data. The blue curves in (d) and (e) are for the STEM-determined sample configuration, allowing fully for the nonuniformity of some bilayer thicknesses, and the red curve in (d) is for the ideal sample configuration. (see Supplemental Material [18]).

(see Supplemental Material [18]) and used as inputs for YXRO. In Fig. 3, we show various results from these simulations. Figure 3(a) shows the calculated SW electric-field strength $|E(z, \theta_{\rm inc})|^2$ as a function of depth and $\theta_{\rm inc}$, including a layer of CO_x-containing surface contaminants. This plot illustrates the scan of the SW vertically in the sample, and makes it clear that the SW has the principal effect of enhancing the RIXS signal from the first LSCO-top/LSMO-bottom interface over the lower-lying LSCO layers and interfaces. Figure 3(b) shows the model structure on which simulations have been carried, focusing in particular on the first interface. The simulated RCs arising from these different regions are shown in Fig. 3(c). It is clear that the calculated RCs for the different depths (Δz) are markedly different. For example, the RC from the LSMO-top/LSCO-bottom interface ($\Delta z = 0$ Å) has a minimum at ~7.9°, while that from the LSCO-top/LSMO-bottom interface ($\Delta z = 22.5$ Å) has a minimum at 8.5° to 9.0°. We determine depth distribution of each RIXS by comparing its experimental RC to a weighted sum of these depth-resolved RCs (depth step of 2.5 Å) until the best fit to the experimental results is found. This has been done both using least-squares fittings and visual inspection of the calculated RCs to the experimental data. Comparing these simulations to the *dd* experimental data in Fig. 2(c), we find that the experimental RCs match the average of the RCs from the whole LSCO layer in Fig. 3(c), as shown by the solid curves. We can thus conclude that all three *dd* excitations show very similar behavior, with profiles suggesting that this part of the RIXS spectrum is quite independent from the position inside the LSCO layer, as indicated by the inset in Fig. 2(c).

We now consider the RCs of the quasielastic and magnetic excitations, as shown in Fig. 2(b). The excitations in this range are more complex to analyze since the magnetic excitations lie very close to the phonon peaks and the elastic zero-loss line, and are also relatively weak. The quasielastic peak includes

the elastic zero-loss line and phonon excitations [19–21,23]. To avoid spurious intensity variations in the fittings, we thus report in Fig. 2(d) RCs as more statistically accurate sums over the peak fitting groups in Fig. 2(b), that is, over elastic + phonon + biphonon and over magnon + bimagnon. For the quasielastic RC that shows minima at ∼8.4°, the depth distribution agrees with the calculated curves which have their origin over most of the LSCO layer (20 Å), excluding the top interface region [see the bottom inset in Fig. 2(d)]. The RCs of the summed magnetic excitations show a similar behavior as the *dd* excitations, but with smaller intensity modulation (∼8%) and minimum at 8.2°. Again, we compare the experimental RC of magnetic excitations to a weighted sum of the simulations in Fig. 3(c) to determine its depth distribution, and this yields the conclusion of a depth distribution peaked at the LSMO-top/LSCO-bottom and LSCO-bottom/LSMO-top interface. We have carried out various simulations by summing over the depth-resolved RC curves to compare with the experimental data, which includes summing over the whole LSCO layer, summing from the bottom LSCO interface, summing from the top LSCO interface, and summing over from both top and bottom LSCO/LSMO interfaces. The experimental RC of magnetic excitations agrees best with the sum of the calculated top-8-Å and bottom-8-Å curves: we interpret this as an enhancement of the magnetic signal at the interfaces, as sketched in the top inset in Fig. 2(d).

In order to more quantitatively determine the depth profiles of various excitations, the experimental RCs have been fit by

$$I^{\mathrm{Expt}}_{\mathrm{RC},j}(\theta_{\mathrm{inc},k}) = \sum_{z_i} W_{ji}(z_i,\theta_{\mathrm{inc},k}) I^{\mathrm{Calc}}_{\mathrm{RC},j}(z_i,\theta_{\mathrm{inc},k}) \times \exp(-z_i/\Lambda_{x,\mathrm{eff}}), \quad (2)$$

where $I^{\mathrm{Expt}}_{\mathrm{RC},j}(\theta_{\mathrm{inc},k})$ is an experimental RC at incidence angle (with j = magnetic or quasielastic, for example), $I^{\mathrm{Calc}}_{\mathrm{RC},j}(z_i,\theta_{\mathrm{inc},k})\exp(-z_i/\Lambda_{x,\mathrm{eff}})$ is one of the calculated RCs in Fig. 3(c) below, and $W_{ji}(z_i,\theta_{\mathrm{inc},k})$ is a weighting coefficient in a fitting procedure that we have derived using the quasi-Newtonian Broyden-Fletcher-Goldfarb-and Shanno (BFGS) method [30]. Finally, plotting the summed amplitudes of these weighting factors at a given z_i interval of 2.5 Å as $W^{\mathrm{Sum}}_{ji}(z_i) = \sum_{\theta_{\mathrm{inc},k}} W_{ij}(z_i,\theta_{\mathrm{inc},k})$ then yields a quantitative estimate of the depth distributions. For example, the magnetic excitations in Fig. 2(e) are found to occupy about 3 Å near the LSMO-top/LSCO-bottom interface, with a weaker contribution also from the next LSCO-top/LSMO-bottom interface. The quasielastic excitation in Fig. 2(f) is found to show contributions from the full LSCO layer, although weighted away from the top interface. The results agree with the more qualitative fitting described above.

This result that shows the depth distribution of magnetic excitations mainly originates from 3–8 Å interfacial regions in LSCO is far from trivial. We note that the magnon excitations seen in RIXS correspond to damped spin waves from the 2D antiferromagnetic lattice in the CuO_2 planes. Upon hole doping, the magnon energy is unchanged but the damping grows and the bimagnon contributions are progressively washed out [31]; therefore, a stronger overall magnetic RIXS intensity at the interfaces might be explained by the charge transfer from LSMO to LSCO that locally reduces the hole doping of the cuprate. This result complements what had been found by studying the x-ray absorption spectra and the magnetic circular dichroism of these LSCO/LSMO interfaces, that a weak ferromagnetic order is induced in the cuprate by the manganite: we conclude thus that the latter does not reduce but, on the contrary, enhances the antiferromagnetic short-range correlation of the cuprate.

As a final aspect of the experimental data, in the Supplemental Material [18] we discuss analogous SW-RIXS results for the structurally less well-defined multilayer grown on TiO_2-terminated STO. These include complementary SW photoemission (SW-XPS) measurements at exactly the same photon energy. Although the stacking sequence of bilayers is not regular in this sample, and this strongly influences the SW form, the SW-RIXS results are in qualitative agreement with those for SrO-terminated growth, but also suggest that the d_{z2} *dd* excitation is slightly enhanced at the LSCO-top/LSMO-bottom interface, possibly signaling a local modification of the crystal field, i.e., of the Cu^{2+} ion coordination. The SW-XPS RCs for Cu 3*p* and Mn 3*p* RCs (Fig. S9 [18]) are found to be well predicted by YXRO calculations for the best-fit geometry. Thus, these additional SW-RIXS and SW-XPS results for a less ideal sample configuration further confirm our analysis of the SW-RIXS data for SrO-terminated growth, and suggests differences in depth within the *dd* excitations, but future measurements with a better sample will be needed to confirm this.

In conclusion, we have demonstrated that soft x-ray RIXS is sensitive to standing waves. For the LSCO/LSMO multilayer heterostructures, thanks to advanced x-ray optical theoretical simulations, we could interpret qualitatively the experimental results in terms of relative enhancement of some of the excitations at the interfaces and with respect to the bulk regions of LSCO. In particular, we found that for the sample grown on an SrO-terminated STO substrate, the magnetic excitations have their origin from both the top and bottom LSCO/LSMO interfaces. Future studies with superlattices of more ideal geometry should permit more quantitatively determined RIXS depth distributions, including differences in the *dd* excitations. Applying SW-RIXS to quasi-2D quantum materials (e.g., topological insulators and transition-metal dichalcogenides) is also promising, with the SW in these systems resulting from Bragg reflection from different crystal planes, and RIXS thus in principle being given atomic-layer sensitivity. Although there are at present no theoretical simulations of RIXS that take account of the depth of excitations, we suggest that future measurements of this type on more regular sample configurations will stimulate them, and that SW-RIXS will open up a new spatial dimension to this already powerful technique.

This work was supported by the US Department of Energy under Contract No. DE-AC02- 05CH11231 (Advanced Light Source), and by US DOE Contract No. DE-SC0014697 through the University of California Davis (C.-T.K., S.C.L., and C.S.F.). C.S.F. has also been supported by the Director, Office of Science, Office of Basic Energy Sciences (BSE), Materials Sciences and Engineering (MSE) Division, of the US Department of Energy under Contract No. DE-AC02-05CH11231, through the Laboratory Directed

Research and Development Program of Lawrence Berkeley National Laboratory, through a US DOE BES MSE grant at the University of California Davis from the X-Ray Scattering Program under Contract No. DE-SC0014697, through the APTCOM Project, "Laboratoire d'Excellence Physics Atom Light Matter" (LabEx PALM) overseen by the French National Research Agency (ANR) as part of the "Investissements d'Avenir" program, and from the Jűlich Research Center, Peter Grűnberg Institute, PGI-6. J.V. and N.G. acknowledge funding through the GOA project "Solarpaint" of the University of Antwerp. The microscope used in this work was partly funded by the Hercules Fund from the Flemish Government. The RIXS experiment was made at the beam line ID32 of the ESRF using the ERIXS spectrometer. G.G. and Y.Y.P. were supported by the ERC-P-ReXS Project No. 2016-0790 of the Fondazione CARIPLO and Regione Lombardia, Italy.

[1] A. Kotani and S. Shin, Rev. Mod. Phys. **73**, 203 (2001).
[2] L. J. P. Ament, M. van Veenendaal, T. P. Devereaux, J. P. Hill, and J. van den Brink, Rev. Mod. Phys. **83**, 705 (2011).
[3] S.-H. Yang, A. X. Gray, A. M. Kaiser, B. S. Mun, B. C. Sell, J. B. Kortright, and C. S. Fadley, J. Appl. Phys. **113**, 073513 (2013).
[4] A. Ohtomo and H. Y. Hwang, Nature (London) **427**, 423 (2004).
[5] S. Stemmer and S. J. Allen, Annu. Rev. Mater. Res. **44**, 151 (2014).
[6] B. W. Batterman and H. Cole, Rev. Mod. Phys. **36**, 681 (1964).
[7] M. J. Bedzyk, D. Bilderback, J. White, H. D. Abruna, G. M. Bommarito, J. Phys. Chem. **90**, 4926 (1986).
[8] S. K. Ghose and B. N. Dev, Phys. Rev. B **63**, 245409 (2001).
[9] I. A. Vartanyants and M. V. Kovalchuk, Rep. Prog. Phys. **64**, 1009 (2001).
[10] A. Gupta, D. Kumar, and C. Meneghini, Phys. Rev. B **75**, 064424 (2007).
[11] J. Zegenhagen and A. Kazimirov, *The X-ray Standing Wave Technique: Principles and Applications* (World Scientific, Singapore, 2013).
[12] C. S. Fadley, J. Electron Spectrosc. **178-179**, 2 (2010).
[13] C. S. Fadley, J. Electron Spectrosc. **190**, 165 (2013).
[14] A. X. Gray, J. Electron Spectrosc. **195**, 399 (2014).
[15] C. S. Fadley and S. Nemšák, J. Electron Spectrosc. **195**, 409 (2014).
[16] G. M. De Luca, G. Ghiringhelli, C. A. Perroni, V. Cataudella, F. Chiarella, C. Cantoni, A. R. Lupini, N. B. Brookes, M. Huijben, G. Rijnders, and M. Salluzzo, Nat. Commun. **5**, 5626 (2014).
[17] M. Huijben, Ph.D. dissertation, University of Twente, 2006; http://doc.utwente.nl/55832/1/thesis_Huijben.pdf
[18] See Supplemental Material at http://link.aps.org/supplemental/10.1103/PhysRevB.98.235146 for details on the x-ray optical and structural characterization of the LSCO/LSMO multilayers grown on both TiO_2- and SrO-terminated STO, which includes Refs. [3,32,33].
[19] N. B. Brookes, F. Yakhou-Harris, K. Kummer, A. Fondacaro, J. C. Cezar, D. Betto, E. Velez-Fort, A. Amorese, G. Ghiringhelli, L. Braicovich, R. Barrett, G. Berruyer, F. Cianciosi, L. Eybert, P. Marion, P. van der Linden, and L. Zhang, Nuclear Inst. Method A **903**, 175 (2018).
[20] L. Braicovich, J. van den Brink, V. Bisogni, M. Moretti Sala, L. J. P. Ament, N. B. Brookes, G. M. De Luca, M. Salluzzo, T. Schmitt, V. N. Strocov, and G. Ghiringhelli, Phys. Rev. Lett. **104**, 077002 (2010).
[21] L. Braicovich, M. Moretti Sala, L. J. P. Ament, V. Bisogni, M. Minola, G. Balestrino, D. Di Castro, G. M. De Luca, M. Salluzzo, G. Ghiringhelli, and J. van den Brink, Phys. Rev. B **81**, 174533 (2010).
[22] M. P. M. Dean, R. S. Springell, C. Monney, K. J. Zhou, J. Pereiro, I. Božović, B. Dalla Piazza, H. M. Ronnow, E. Morenzoni, J. van den Brink, T. Schmitt, and J. P. Hill, Nat. Mater. **11**, 850 (2012).
[23] M. Magnuson, T. Schmitt, V. N. Strocov, J. Schlappa, A. S. Kalabukhov and L. Duda, Sci. Rep. **4**, 7017 (2014).
[24] C. Monney, T. Schmitt, C. E. Matt, J. Mesot, V. N. Strocov, O. J. Lipscombe, S. M. Hayden, and J. Chang, Phys. Rev. B **93**, 075103 (2016).
[25] L. Chaix, E. W. Huang, S. Gerber, X. Lu, C. Jia, Y. Huang, D. E. McNally, Y. Wang, F. H. Vernay, A. Keren, M. Shi, B. Moritz, Z.-X. Shen, T. Schmitt, T. P. Devereaux, and W.-S. Lee, Phys. Rev. B **97**, 155144 (2018).
[26] J. van den Brink, Europhys. Lett. **80**, 47003 (2007).
[27] F. Forte, L. J. P. Ament, and J. van den Brink, Phys. Rev. B **77**, 134428 (2008).
[28] G. Ghiringhelli, N. B. Brookes, E. Annese, H. Berger, C. Dallera, M. Grioni, L. Perfetti, A. Tagliaferri, and L. Braicovich, Phys. Rev. Lett. **92**, 117406 (2004).
[29] M. Moretti Sala, V. Bisogni, C. Aruta, G. Balestrino, H. Berger, N. B. Brookes, G. M. De Luca, D. Di Castro, M. Grioni, M. Guarise, P. G. Medaglia, F. Miletto Granozio, M. Minola, P. Perna, M. Radovic, M. Salluzzo, T. Schmitt, K. J. Zhou, L. Braicovich, and G. Ghiringhelli, New J. Phys. **13**, 043026 (2011).
[30] J. Nocedal and S. J. Wright, *Numerical Optimization*, 2nd ed. (Springer, New York, 2006), Sec. 8.1.
[31] Y. Y. Peng, E. W. Huang, R. Fumagalli, M. Minola, Y. Wang, X. Sun, Y. Ding, K. Kummer, X. J. Zhou, N. B. Brookes, B. Moritz, L. Braicovich, T. P. Devereaux, and G. Ghiringhelli, Phys. Rev. B **98**, 144507 (2018).
[32] A. X. Gray, C. Papp, B. Balke, S.-H. Yang, M. Huijben, E. Rotenberg, A. Bostwick, S. Ueda, Y. Yamashita, K. Kobayashi, E. M. Gullikson, J. B. Kortright, F. M. F. de Groot, G. Rijnders, D. H. A. Blank, R. Ramesh, and C. S. Fadley, Phys. Rev. B **82**, 205116 (2010).
[33] N. Gauquelin, K. H. W. van den Bos, A. Béché, F. F. Krause, I. Lobato, S. Lazar, A. Rosenauer, S. Van Aert, and J. Verbeeck, Ultramicroscopy **181**, 178 (2017).